# Degradation of multijunction photovoltaic gridlines induced via thermal cycling

Ryan E. Brock[a], Peter Hebert[b], James Ermer[b], Reinhold H. Dauskardt[a],*

[a] Department of Materials Science and Engineering, Stanford University, Stanford, CA 94305, United States
[b] Spectrolab, Inc., Sylmar, CA 91342, United States

## ARTICLE INFO

## ABSTRACT

A well-known but heretofore uncharacterized failure mechanism in multijunction photovoltaic cells involves the development of cracks in the top cell directly adjacent to metal gridline structures. In this study, we systematically explore the potential evolution of stress, grain size, roughness, and hardness of metal gridlines during thermal cycling as it pertains to top cell cracking behavior. We discover that although top cells are found to crack after many cycles, this is not due to an accumulation of stress or damage, but rather a progression of strain hardening within the metal gridlines due to cyclic plastic deformations, quantified as an increase in hardness of as much as 57%. Furthermore, optical and topological characterization reveals morphology changes at the gridlines' top surfaces, lending some insight to commonly observed bus bar wire-bonding issues. Ultimately this suite of characterization techniques not only reveals the underlying behavior leading to gridline-induced top cell cracking failures in multijunction photovoltaics, but also suggests a route forward for the development of improved gridline materials.

## 1. Introduction

Rapid improvement and cost reduction of concentrator systems has led to increased interest in the development of terrestrial installations using high-efficiency multijunction photovoltaic (PV) cells in recent years [1–3]. While concentrator photovoltaic (CPV) systems have held a clear advantage in conversion efficiency over traditional silicon PV, with efficiencies that have long exceeded 40% and even recently reaching as high as 46% [1,4,5], questions regarding long term reliability remain as availability of field use data is limited [1,6]. Furthermore, environmental degradation is of greater concern as cells are subjected to higher incident flux of UV light and larger temperature cycles.

The application of multijunction PV cells, with their complex layered structures, in terrestrial applications requires an improved understanding of thermomechanical reliability and testing metrologies as the basis for improved lifetime predictions [7]. The ability to establish bankability via accelerated life testing stands as a key hurdle to any new solar technology if it hopes to overcome the relative safety provided by silicon panels [3,8–11].

While there have been studies of performance degradation [12–16], little has been done to understand and quantify the underlying materials properties that lead to degradation. Of particular concern are the effects of thermal cycling, given the large variance in coefficient of thermal expansion between the many individual layers within a multijunction cell [17–19]. A well-known but heretofore uncharacterized failure mechanism involves the development of cracks in the top cell directly adjacent to metal gridline structures [17,18,20]. As shown in Fig. 1, after many thermal cycles, cracks form at the corner of the semiconductor cap, and cells fail due to metal diffusion into these cracks. These cracks only form following multiple thermal cycles (has not been observed following a singular temperature cycle). This implies that cracking is caused by the cycle-by-cycle accumulation of damage within the brittle device layers and substrate. However, as this is unlikely to be the case in a brittle, defect-free material, it follows that there must be a cycle-by-cycle change in stress state of the gridline structure leading to these mechanical failures [21]. Previous work has investigated these failures as a function of current density within CPV cells, implying that there may be a synergistic effect between multiple stressing parameters, but in this case, we will focus on cracks induced by mechanical stress [16].

In this study, we systematically explore the potential evolution of stress, grain size, roughness, and hardness of metal gridlines during thermal cycling as it pertains to top cell cracking behavior. As is fairly typical in multijunction PV systems [20], gridline metals composed primarily of silver are used, and are deposited at a tunable rate,
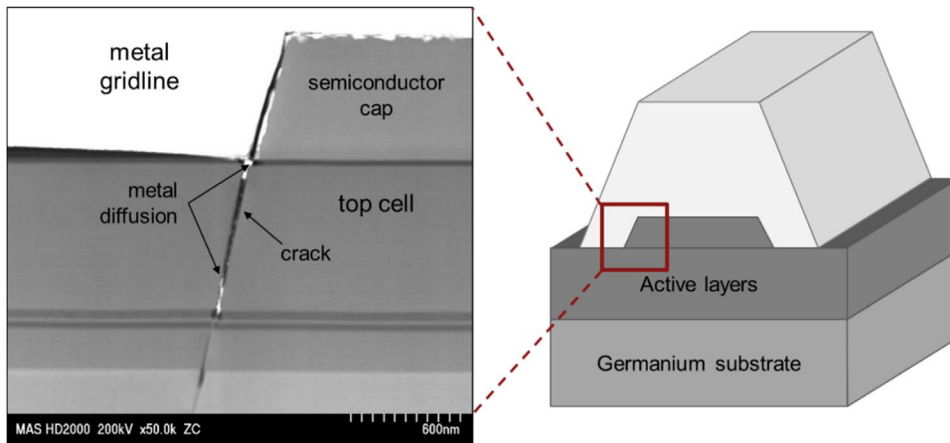
**Fig. 1.** A cross-sectional area of a gridline structure atop a multijunction cell imaged via SEM. This cell has been thermally cycled, causing the top cell to develop a crack originating from the corner of the semiconductor cap, which serves as a catastrophic failure mechanism as metal subsequently diffuses into the cell and shorts it.

allowing for comparison of fast and slow depositions. Thermal cycling conditions were varied including the use of exaggerated temperature extremes in order to accelerate degradation and simulate full lifetimes over the course of 2000 thermal cycles. While this study focuses specifically on one type of gridline structure/photovoltaic system, and it is likely that the development of cracks is specifically enabled by the relatively low fracture toughness of the top cell material (InGaP) [22], the methodologies employed herein can be broadly applied to any photovoltaic with similar geometries and design constraints. Ultimately this suite of characterization techniques reveals the underlying behavior leading to gridline-induced top cell cracking failures in multijunction photovoltaics, paving the way for future engineering to prevent such failures and extend operating lifetimes of these devices.

## 2. Experimental procedures

### 2.1. Metal coating and gridline depositions

Metal layers were deposited atop epitaxially grown multijunction photovoltaic cells on 180 μm germanium substrates (Spectrolab). A schematic of these test structures is shown in Fig. 2. Deposition rates of either 20 Å/s or 50 Å/s were used. Four-inch wafers with blanket coatings and four-inch wafers with patterned gridline structures were created. The wafers with gridline structures each included 11 sets of 250 μm, 100 μm, 25 μm, 15 μm, and 10 μm wide lines, spaced 1 mm apart and approximately 75 mm long. As is typical for these gridline structures, the edges had a slight pitch, on the order of a few micrometers of horizontal run. In all cases, nominal metal thickness was 6 μm. Following deposition, sets of three wafers underwent three different cycling conditions: a control group, a −180 °C to +125 °C cycle, and a −40 °C to +125 °C cycle, for specified durations, at a rate of 20 cycles per day, up to 2000 cycles. Cycling was performed with zero dwell time, resulting in approximate temperature ramp rates of 8 °C per minute. The maximum and minimum temperatures are somewhat in

excess of what would be expected in field exposures, and we therefore expect 2000 cycles to approximately represent an accelerated full lifetime exposure. The draft IEC standard for CPV cell qualification has a requirement of 2000 thermal cycles, while others have suggested a minimum of 500 thermal cycles for full lifetime qualification [23]. Simulation of a full lifetime over a smaller temperature range would require up to 70,000 thermal cycles [6].

### 2.2. Wafer curvature stress measurement

A well-established technique for the measurement of thin film stresses, wafer curvature is used to quantify the residual stress in the blanket coated films following deposition, and subsequently used to quantify the change in residual stress following thermal cycling [24–27]. Wafers are placed into a temperature- and humidity-controlled wafer curvature instrument (FLX-2320, Toho Technology, Chicago, IL) film-side down, and the curvature is measured by using a laser to scan a line across the surface while quantifying the angle of deflection of the reflected light, as shown in Fig. 3. Two measurements of curvature are made for each specimen, orthogonal to one another, and averaged. The film stress is then quantified using Stoney's equation:

$$\sigma_f = \left( \frac{E_s}{1-v_s} \right) \frac{h_s^2}{6h_{met}} \Delta \kappa \, [MPa] \tag{1}$$

where $E_s$, $v_s$, and $h_s$ are the young's modulus, Poisson's ratio, and thickness of the substrate, respectively, and $h_{met}$ is the metal thickness. In order to quantify the residual stress produced strictly by the metal deposition process, wafers with epitaxial layers (no metal) were used as the baseline curvature measurement ($\kappa_o$) for all subsequent measurements, measured for each individual wafer.

### 2.3. Optical grain size characterization

Grain size is measured directly via optical characterization for both
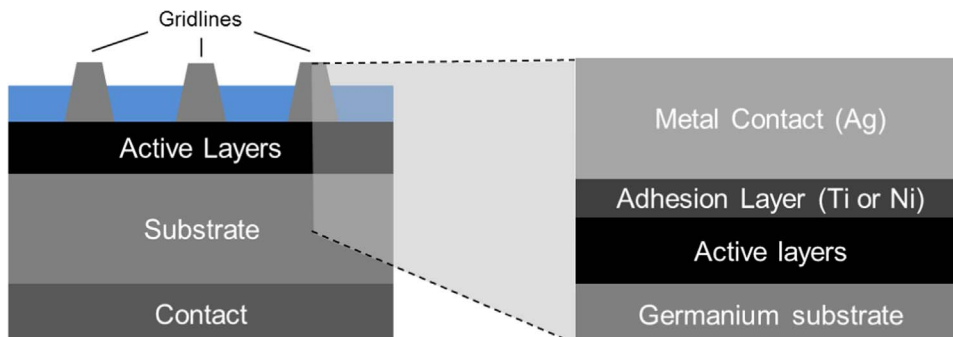


**Fig. 2.** Schematic representation of multijunction solar cell (left), with a schematic of the test structures created for the purposes of this study (right). In the case of wafer curvature specimens, wafers with blanket depositions of each of the layers depicted were prepared.
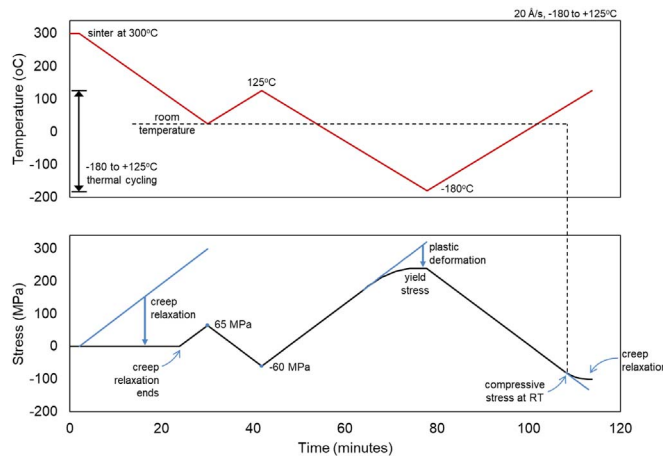
**Fig. 3.** Schematic of drying stress specimen in scanning laser substrate curvature instrument. Note in the actual instrument, the wafer is placed on a stage in the bottom of the chamber, with the laser pointed down at it from above.



**Fig. 4.** Evolution of stress following thermal cycling as evaluated by wafer curvature measurements. All wafers have an initial residual tensile stress from silver/germanium thermal mismatch during cooling from the sintering temperature (300 °C). Compressive stress subsequently develops with increasing cycles.

gridline structures and blanket metal coatings. Grain boundaries in these structures are clearly visible without any etching required. Optical images were captured (Keyence Digital Microscope VHX-500F, Keyence, Osaka, Japan) at $1000\times$ magnification and subsequently processed using ImageJ to calculate average grain size [27]. Strategies for maximizing the effectiveness of such a process are well-documented, but briefly, images were converted to 32-bit, and 'enhanced contrast' and 'bandpass filter' processes were subsequently applied, followed by a threshold filter to create a black/white map of grains vs. grain boundaries. Approx. 100–300 grains were measured in the resulting particle analysis of each image, and average grain size is reported across at least three such images for each specimen considered.

### 2.4. Nanoindentation determination of hardness

Hardness of both gridline structures and blanket metal coatings is investigated in this study using nanoindentation techniques. Measurements were made with a nanoindenter (iNano, Nanomechanics, Inc., Oak Ridge, TN) fitted with a Berkovich indenter tip [28]. All measurements are performed with identical maximum indentation load (45 mN) and strain rate (0.2% per second). Hardness is calculated using the projected indent area obtained from the known tip-area function ($A_c$) for the indenter tip and the relation:

$$H = \frac{P}{A_c} \, [\text{GPa}] \tag{2}$$

where H is hardness and P is the applied load.

### 2.5. Atomic force microscopy

Topographical maps of the surface features of the metal gridline structures are obtained using non-contact atomic force microscopy (NC-AFM) (XE-70 microscope, Park Systems, Santa Clara, CA) in order to quantify surface roughness. The system is fitted with a 50 μm scanner, allowing for a maximum measurement area of 45 μm × 45 μm when using a 10% overscan. We note here that vertical feature sizes on the

order of a micron or more in height in some images necessitates the use of high gain (in turn producing a small amplitude of high frequency noise) as well as artifact removal. Ten-point mean roughness is used to quantify the height of the tallest features within the image by taking the average difference between the ten highest and ten lowest points in each line scan. Regions to be measured are chosen at random, and several regions are examined for each specimen, in order to avoid over- or under- sampling of grain boundaries.

## 3. Results and discussion

### 3.1. Stress evolution via thermal cycling

Given the initial hypothesis, that gridlines develop and store additional mechanical stress as they are thermally cycled, we first examine the stress measurements presented in Fig. 4 obtained via wafer curvature measurements. In this case, we are not directly examining the stress in gridline structures, but rather are using blanket metal coatings which should develop the same thermal stresses and which allow the use of the wafer curvature method. From the equation for thermal mismatch,

$$\sigma_f = E_f \Delta\alpha \Delta T \, [\text{MPa}] \tag{3}$$

where $\sigma_f$ is the film stress, $E_f$ is the film modulus, $\Delta\alpha$ is the difference in thermal expansion coefficient (19.5 for Ag, 6.1 for Ge) [29], and $\Delta T$ is the change in temperature, the silver film is expected to develop a large tensile residual stress as it cools from the sintering temperature (300 °C) to room temperature. However, creep behavior allows for relaxation of these stresses when at appropriately high temperatures, and thus we only measure initial residual stresses of 64.2 MPa and 47.1 MPa for the 20 Å/s and 50 Å/s films, respectively.

After as few as 100 thermal cycles, a significant change in residual film stress is observed, as all films considered developed compressive stress. In the case of the −180 °C to +125 °C cycling condition, the overall magnitude of stress has even flipped to compressive. The following measurements at 500, 1000, and 2000 cycles show that film stress continues to change, albeit much more slowly, and also reveals that the stress appears to be more dependent upon the temperature cycling conditions than upon the initial stress conditions, as the wafers cycled under the same conditions converged toward one another. As the overall magnitude of stress shows a decrease with thermal cycling (only −18.2 to +8.9 MPa after 2000 cycles), rather than the hypothesized increase, it becomes apparent that other behavior must be responsible for degradation.

**Fig. 5.** Step-by-step analysis of the predicted stress evolution within a blanket metal film during the first thermal cycle. Thermal mismatch would predict a very high tensile stress to develop during initial cooling from sintering (indicated in light blue), but creep relaxation prevents this until the temperature falls below the creep relaxation temperature. From the initial tensile stress at room temperature, an increase in temperature leads to compressive stress in the film, but a nonlinearity occurs when cycling down to negative temperatures, as the expected thermal mismatch stress (again in light blue) exceeds the yield stress. Upon the next cycle to high temperature, creep relaxation again takes place, and so with each additional cycle, films undergo further plastic deformation at low temperatures, followed by relaxation at high temperatures. (For interpretation of the references to color in this figure legend, the reader is referred to the web version of this article.)

Further examination of the stresses expected to develop due to thermal mismatch during these thermal cycles, as shown in Fig. 5 reveals an explanation for this observed development of compressive stresses. With each thermal cycle, the metal films are plastically deforming at low temperatures (hardening), leading to a compressive stress when returning to room temperature. Then the high temperatures

on the opposite end of the thermal cycle allow for creep relaxation, which in turn leads to further plastic deformation when cooled again. Thus we've found the likely source of accumulated change-of-state in the system, not in the stored residual stresses at room temperature, but rather in the hardness of the metals.

### 3.2. Morphological effects of thermal cycling on gridline structures

As the gridline structures were deposited with two different deposition rates, it was initially expected that they may have different initial grain sizes and therefore different mechanical properties. This is confirmed in Fig. 6, in which it is shown that the 50 Å/s and 20 Å/s films had average initial grain diameters of 9.5 μm and 13.3 μm, respectively. Note that since many of the visible grains are greater than 6 μm in diameter, the thickness of the lines, it is likely that 2D optical characterization of grain size somewhat overestimates three-dimensional grain size. Referring now back to the initial residual stress measurements, it is apparent that the creep relaxation behavior, which is a grain boundary-enabled process, was able to relieve more stress in the 50 Å/s films due to the difference in grain size [30].

As cycling proceeds, grain size appears to decrease slightly, which could be relevant to any potential evaluation of hardness. Unlike the case of the stress evolution, here the final grain size after 2000 cycles looks to be largely dependent upon the initial grain size and the number of cycles, and not on the temperature range. Given that the different cycling temperatures had very little impact, it is evident that the change in grain size is largely due to deformation of the films, not any thermally activated effects.

Additionally, there is an optically evident increase in roughness of the top surface of these metal gridlines following cycling, as the grain boundaries very clearly become more pronounced in the top-right image of Fig. 6 (as compared to top-left). This is further investigated through the use of AFM images, shown in Fig. 7. Moving from left to right, and noting that all images are shown on the same height scale, we
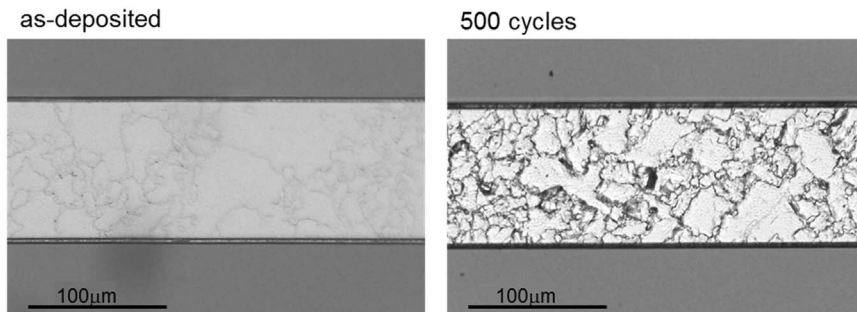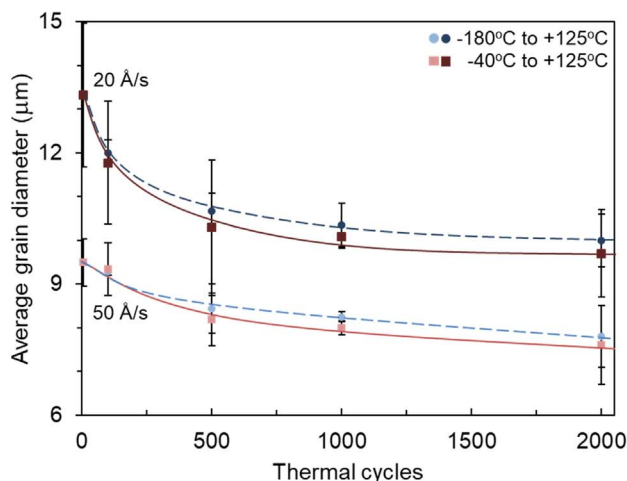
**Fig. 6.** (top) Optical images used in grain size analysis. Grain boundaries are slightly raised above the surface. (bottom) Average grain sizes as evaluated throughout thermal cycling. Each point represents average grain size obtained from at least three different regions, each with > 100 visible grains.
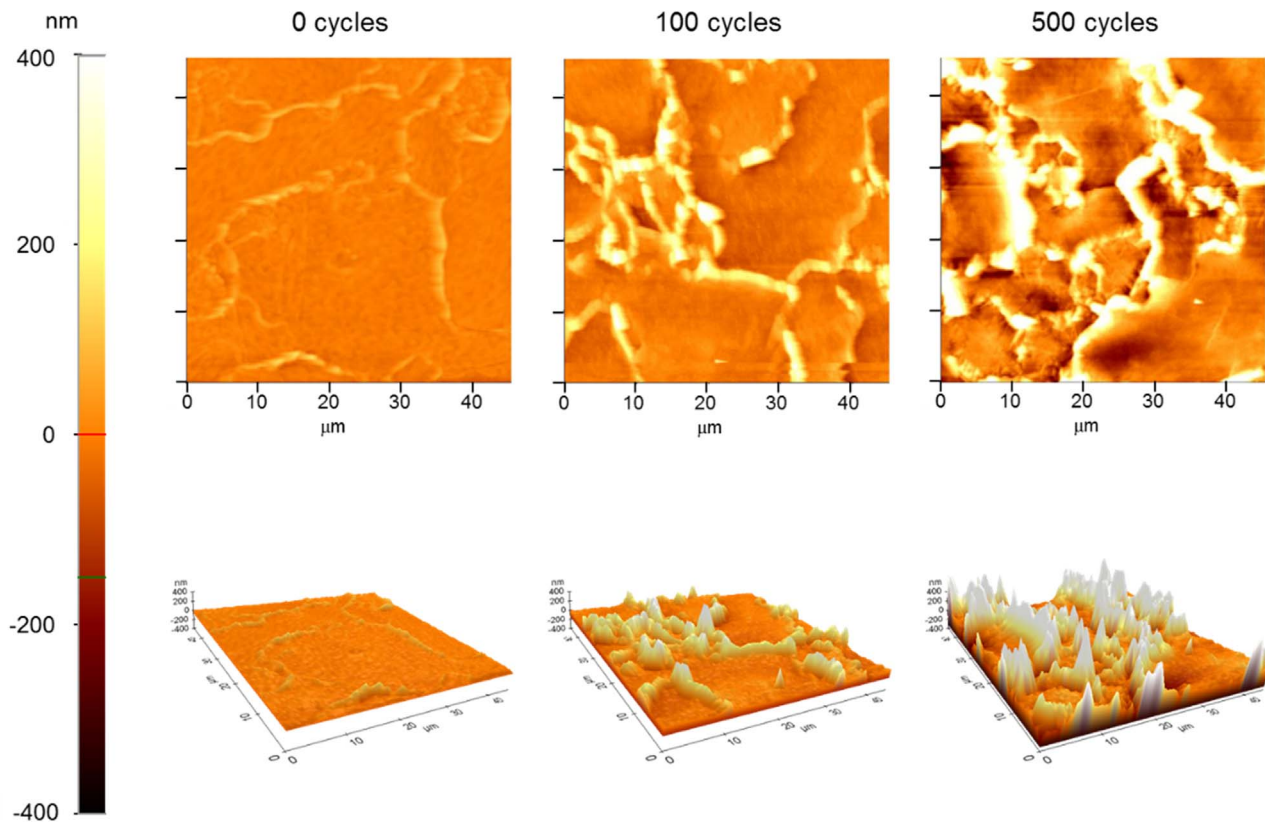
**Fig. 7.** A series of atomic force microscopy images obtained from the same wafer following 0, 100 and 500 thermal cycles from −180 to +125 °C. All images are 45 μm × 45 μm and displayed with the same scale in all dimensions (z-scale shown at left). Bottom row images are 3D representations of top row images.
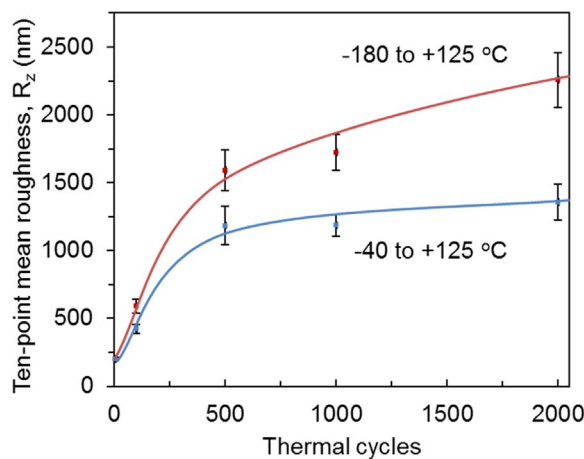


**Fig. 8.** Ten-point mean roughness as obtained from atomic force microscopy images. Roughness for the two deposition conditions is negligibly different, and the data are therefore combined based on cycling temperatures. Each point represents $R_z$ values obtained from at least three separate 45 μm × 45 μm regions.

observe that grain boundary heights are initially quite small, on the order of 100 nm raised above the surface. After just 100 cycles, these have more than doubled in height, and finally with 500 thermal cycles, grain boundary heights have again more than doubled. This is especially evident in the 3D representations. This effect is then quantified as ten-point mean roughness in Fig. 8, where again the behavior is clearly dependent upon cycling temperature. For the −180 °C to +125 °C cycling condition, $R_z$ increases from the initial 200 nm up to over 2200 nm, while the $R_z$ for the −40 °C to +125 °C cycling condition increases up to nearly 1400 nm.

The increase in surface roughness is likely originating from the

plastic deformation of the gridlines, as they compress when returning to room temperature and push material upward at the grain boundaries, and as grains shear past one another. While not strictly related to the hardening or top cell cracking behaviors, this does have important implications for another known degradation mechanism within cells [8]. Wire-bonding is used to electrically connect to the larger gridlines, also known as bus bars, and as roughness increases, the initially strong wire-bonds can become weakened and more resistive. This is likely due to precisely the effect we have characterized here, in which the changing surface morphology of the gridline is also impacting any bonds made to that top surface.

### 3.3. Hardening of metal gridlines via thermal cycling

Initial comparison of hardness values in Fig. 9 shows a higher hardness in the 50 Å/s gridlines, as would be expected from the grain boundary strengthening effect and given the smaller grain size in 50 Å/s gridlines than in 20 Å/s gridlines. This is true across all line widths considered (250, 100, 25, 15, and 10 μm), though we note that for the 15 μm and 10 μm lines, a significantly lower value of hardness is measured, with hardness values on the order of 0.60 GPa for the wider lines and as low as 0.18 GPa for the thinnest lines. This is due to inaccuracies in the projected contact area ($A_c$) as the indent size approaches the size of the line itself, positioning inaccuracy of indent sites, as well as constraint of the plastic zone surrounding the indentation site. Based on these measurements, it is apparent that the plastic zone size is on the order of 15–25 μm in size, as the 25, 100, and 250 μm line widths all produced remarkably consistent hardness measurements.

As was predicted in the initial stress analysis of Fig. 5, there is a large accumulation of plastic deformation in these gridline structures during thermal cycling. Yield strength can be approximated as equal to
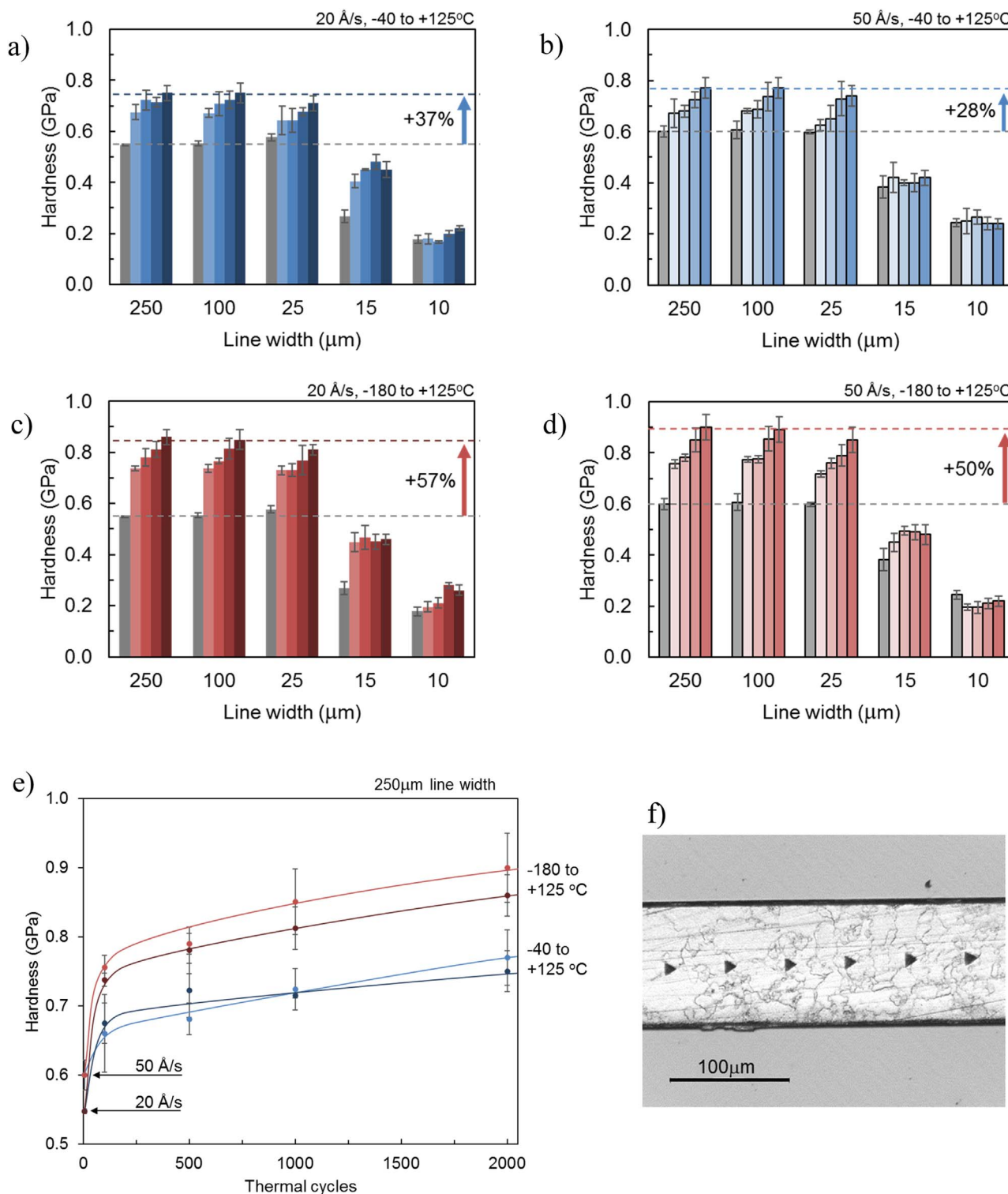
**Fig. 9.** (a)-(d) Hardness measurements for each of the gridline structures considered. In each plot, the left-most gray bar in each group represents the baseline hardness (no cycling), and each subsequent darker colored bar is hardness measured at each time break (breaks at 250, 500, 1000, and 2000 cycles). Each bar represents between three and nine nanoindentation measurements of hardness. (e) Characteristic hardness vs. thermal cycles behavior is demonstrated for the 250 μm wide lines. (f) Optical image of representative indents produced in the surface of a 100 μm wide line shows relative scale of indents vs. line width. (For interpretation of the references to color in this figure legend, the reader is referred to the web version of this article.)

one-third the value of measured hardness, or about 185 MPa in this case, which fits well with the expected stress ranges shown in our stress analysis. The subsequent increases in hardness during thermal cycling between 28–57% serve to quantify this large accumulation of plastic deformation. Also, as was observed in the wafer curvature

measurements, the final value of hardness following 2000 cycles is much more dependent upon temperature cycling conditions than it is upon the initial hardness value. For the −40 to +125 °C cycling condition, final hardness values are as high as 0.77 GPa, and the −180 to +125 °C cycling condition produces hardness values as high as

0.90 GPa. Though most of this hardness increase occurs within the initial 100 cycles, we observe for both cycling conditions that hardness is continuing to increase even after 2000 thermal cycles.

Finally returning to the initial impetus for this work, we have accumulated enough evidence to discern the cause of gridline-induced top cell cracking in multijunction PV. As gridlines are thermally cycled, the stored residual stress at room temperature does not increase, but rather decreases. However, each cycle plastically deforms the gridlines, effectively work hardening them with each additional thermal cycle. Previous work on Metal-Ceramic joints has shown how this sort of work hardening effect can dramatically increase the stress at an interface between a metal line and a rigid substrate [31]. This effect has been observed both in finite element simulations as well as in experimental studies [31,32]. Additionally, the geometry of the metal gridlines contains a sharp corner between the gridline and underlying substrate, which can lead to a stress-concentration factor of up to 10x at the edge of the metal-semiconductor interface [33]. This means that eventually, when cycled to one of the thermal extremes, the thermal mismatch strain between gridline and substrate leads to much higher stored stresses (whereas before, it would lead to yielding of the metal). Between the combined effects of accumulated work-hardening of the metal due to thermal mismatch and the stress concentration effect, the stress reaches a high enough point to overcome the fracture strength of the top-cell semiconductor. Ultimately, there is a trade-off between gridline peeling and semiconductor fracture: thicker gridlines are able to accommodate greater thermal strains, and are less likely to peel. But these thicker gridlines also store sufficient strain energy to induce cracking in the underlying semiconductor. This suggests that improving gridline adhesion through other strategies, and thus allowing the use of thinner gridlines, could be the best possible path forward for improved reliability of metal gridlines. While this study has focused on the use of evaporated silver gridlines, the results should be broadly applicable as the industry moves forwards to other emerging metallizations. As necessary, this work may be easily reproduced for other metallizations either experimentally or using known strain-hardening parameters.

## 4. Conclusions

The discovery of the underlying mechanism behind thermal cycling failures at the gridline-semiconductor interface in multijunction photovoltaics is yet another step towards the goal of extended operating lifetimes for terrestrially deployed MJPV systems. We were able to dispel the previously held notion that this cracking was induced via either some fatigue mechanism or via accumulation of high residual stress within the cell, and found that the cause of fracture is likely a combined effect of the work hardening of gridline structures and the stress concentration at the sharp corner formed by the semiconductor cap layer. Hardness increases of over 50% were measured in the most extreme cases examined. Exposure to larger temperature ranges accelerates this increase in hardness, lending credence to the ability to perform accelerated full-lifetime tests using elevated stressing parameters. This information will allow for much more robust design for reliability in multijunction cells, fostering wider adoption of CPV technologies.

## Acknowledgements

## References

[1] H. Cotal, C. Fetzer, J. Boisvert, G. Kinsey, R. King, P. Hebert, H. Yoon, N. Karam, III–V multijunction solar cells for concentrating photovoltaics, Energy Environ. Sci. 2 (2009) 174–192.

[2] M. Bosi, C. Pelosi, The potential of III-V semiconductors as terrestrial photovoltaic devices, Progress. Photovolt.: Res. Appl. 15 (2007) 51–68.

[3] D.J. Friedman, R.R. King, R.M. Swanson, J. McJannet, D. Gwinner, Editorial: toward 100 gigawatts of concentrator photovoltaics by 2030, IEEE J. Photovolt. 3 (2013) 1460–1463.

[4] R.R. King, A. Boca, W. Hong, X.Q. Liu, D. Bhusari, D. Larrabee, K.M. Edmondson, D. C. Law, M. Fetzer, S. Mesropian, N.H. Karam, Band-gap-engineered architectures for high-efficiency multijunction concentrator solar cells, in: Proceedings of the 24th European Photovoltaic Solar Energy Conference and Exhibition, 2009, pp. 1–7.

[5] T.N.D. Tibbits, P. Beutel, M. Grave, C. Karcher, E. Oliva, G. Siefer, A. Wekkeli, M. Schachtner, F. Dimroth, A.W. Bett, R. Krause, M. Piccin, N. Blanc, M. Muñoz-rico, C. Arena, E. Guiot, C. Charles-alfred, C. Drazek, New efficiency frontiers with wafer-bonded multi-junctions solar cells, in: Proceedings of the European PV Solar Energy Conference and Exhhibition, 2014, pp. 1–4.

[6] P.J. Verlinden, A. Lewandowski, C. Bingham, G.S. Kinsey, R.A. Sherif, J.B. Lasich, Performance and reliability of multijunction III-V modules for concentrator dish and central receiver applications, in: Proceedings of the Conference Record of the 2006 IEEE 4th World Conference on Photovoltaic Energy Conversion, WCPEC-4, 1, 2007, pp. 592–597.

[7] G.S. Kinsey, K.M. Edmondson, Spectral response and energy output of concentrator multijunction solar cells, Progress. Photovolt. 17 (2009) 279–288.

[8] M.A. Quintana, D.L. King, T.J. McMahon, C.R. Osterwald, Commonly observed degradation in field-aged photovoltaic modules, in: Proceedings of the Conference Record of the Twenty-Ninth IEEE Photovoltaic Specialists Conference, 2002, 2002, pp. 1436–1439.

[9] A.M. Reis, N.T. Coleman, M.W. Marshall, P.A. Lehman, C.E. Chamberlin, Comparison of PV module performance before and after 11-years of field exposure, in: Proceedings of the Conference Record of the Twenty-Ninth IEEE Photovoltaic Specialists Conference, 2002, 2002, pp. 1432–1435.

[10] D.L. King, Ma Quintana, Ja Kratochvil, D.E. Ellibee, B.R. Hansen, Photovoltaic module performance and durability following long-term field exposure, AIP Conf. Proc. (1999) 565–571.

[11] C. Algora, P. Espinet, M. Vázquez, N.S. Bosco, D.C. Miller, S.R. Kurtz, F. Rubio, R. McConnell, Reliability, in: Handbook of Concentrator Photovoltaic Technology, John Wiley & Sons Inc, Hoboken, 2016.

[12] I.A. Rey-Stolle Carlos, High-irradiance degradation tests on concentrator GaAs solar cells, Progress. Photovolt.: Res. Appl. 11 (2003) 249–254.

[13] C. Algora, Reliability of III-V concentrator solar cells, Microelectron. Reliab. 50 (2010) 1193–1198.

[14] J.A. Tsanakas, M. Karoglou, E.T. Delegou, P.N. Botsaris, A. Bakolas, A. Moropoulou, Assessment of the Performance and Defect Investigation of PV Modules after Accelerated Ageing Tests, in: Proceedings of the International Conference on Renewable Energies and Power Quality, Bilbao, Spain, 2013.

[15] J.A. Tsanakas, M. Sicre, C. Carriere, R. Elouamari, A. Vossier, J.-E. de Salins, B. Levrier, A. Dollet, A novel approach of accelerated aging tests for high concentration III–V multijunction solar cells through rapid irradiation/thermal cycles, Sol. Energy 116 (2015) 205–214.

[16] V. Orlando, M. Gabas, B. Galiana, P. Espinet-Gonzalez, S. Palanco, N. Nunez, M. Vazquez, K. Araki, C. Algora, Failure analysis on lattice matched GaInP/Ga (In)As/Ge commercial concentrator solar cells after temperature accelerated life tests, Progress. Photovolt. 25 (2017) 97–112.

[17] N. Bosco, Reliability concerns associated with PV technologies, Nrel (2010) 1–11.

[18] N.G. Dhere, Reliability of PV modules and balance-of-system components, in: Proceedings of the Conference Record of the IEEE Photovoltaic Specialists Conference, 2005, pp. 1570–1576.

[19] J. Yang, Z. Peng, D. Cheong, R. Kleiman, Fabrication of high-efficiency III-V on silicon multijunction solar cells by direct metal interconnect, IEEE J. Photovolt. 4 (2014) 1149–1155.

[20] T.K. Wen, C.C. Yin, Crack detection in photovoltaic cells by interferometric analysis of electronic speckle patterns, Sol. Energy Mater. Sol. Cells 98 (2012) 216–223.

[21] A.G. Evans, Fatigue in ceramics, Int. J. Fract. 16 (1980) 485–498.

[22] G. Michot, A. George, A. Chabli-Brenac, E. Molva, Fracture toughness of pure and in-doped GaAs, Scr. Metall. 22 (1988) 1043–1048.

[23] Wohlgemuth, S. Kurtz, Photovoltaic Module Qualification Plus Testing, in: Proceedings of the IEEE 40th Photovoltaic Specialist Conference, 2014, pp. 3589–3594.

[24] M.F. Doerner, D.S. Gardner, W.D. Nix, Plastic properties of thin films on substrates as measured by submicron indentation hardness and substrate curvature techniques, J. Mater. Res. 1 (1986) 845–851.

[25] P.A. Flinn, Principles and applications of wafer curvature techniques for stress measurements in thin films, Mater. Res. Soc. Symp. Proc. 130 (1989) 41–51.

[26] A. Lee, C.S. Litteken, R.H. Dauskardt, W.D. Nix, Comparison of the telephone cord delamination method for measuring interfacial adhesion with the four-point bending method, Acta Mater. 53 (2005) 609–616.

[27] M.D. Abràmoff, P.J. Magalhães, S.J. Ram, Image processing with imageJ, Biophotonics Int. 11 (2004) 36–41.

[28] M. Khrushchov, E. Berkovich, Methods of determining the hardness of very hard materials: the hardness of diamond, Ind. Diam. Rev. 11 (1951) 42–49.

[29] Engineering Toolbox, 〈http://www.engineeringtoolbox.com/linear-expansion〉.

[30] R.L. Coble, A model for boundary diffusion controlled creep in polycrystalline materials, J. Appl. Phys. 34 (1963) 1679–1682.

[31] S.P. Kovalev, P. Miranzo, M.I. Osendi, Finite element simulation of thermal residual stresses in joining ceramics with thin metal interlayers, J. Am. Ceram. Soc. 81 (1998) 2342–2348.

[32] B.J. Dalgelish, M.C. Lu, A.G. Evans, The strength of ceramics bonded with metals, Acta Metall. 36 (1988) 2029–2035.

[33] R.E. Peterson, R. Plunkett, Stress concentration factors, J. Appl. Mech. 42 (1975) 248.